3D Bioprinting of a GelMA/COS Dermal Scaffold for Full-Thickness Skin Tissue Regeneration

Lu Han[a], Zixian Liu[a, b], Meng Li[a, c], Zhizhong Shen[a, d], Shengbo Sang*[a, b] and Jianming Wang*[e].

a Shanxi Key Laboratory of Micro Nano Sensors & Artificial Intelligence Perception, College of Electronic Information and Optical Engineering, Taiyuan University of Technology, Taiyuan 030024, China

b Key Lab of Advanced Transducers and Intelligent Control System of the Ministry of Education, Taiyuan University of Technology, Taiyuan 030024, China

c Shanxi-Zheda Institute of Advanced Materials and Chemical Engineering, Taiyuan 030024, China

d Shanxi Research Institute of 6D Artificial Intelligence Biomedical Science, Taiyuan 030031, China

e General Hospital of TISCO, North Street, Xinghualing District, Taiyuan 030809, PR China, No. 213 Beidajie, Xinghualing District, Taiyuan, Shanxi 030809, P. R. China

* Correspondence: sunboa-sang@tyut.edu.cn

Abstract

Dermal substitutes have provided a template for the regeneration and reconstruction of the dermis. However, the healed skin tissue often exhibits abnormal morphology and functionality, including scarring and inflammation. In this research, a composite bioink composed of methacrylated gelatin (GelMA) and chitosan oligosaccharide (COS) was proposed for printing a dermal scaffold using Digital Light Processing (DLP) technology. The GelMA/COS bioink exhibited suitable porosity, swelling, degradation rate, and mechanical properties. The inclusion of COS demonstrated antibacterial effects against both gram-positive and gram-negative bacteria, while simultaneously fostering the proliferation of human dermal fibroblasts (HDFs). Additionally, the application of COS could effectively reduce the expression levels of fibrosis-related genes, such as collagen I, collagen III and fibronectin I. The 3D-printed cell-laden dermal scaffold exhibited excellent shape fidelity and high cellular viability, facilitating the extension of HDFs along the scaffold and simultaneous secretion of ECM protein. Furthermore, the HDFs-laden dermal scaffold was transplanted into the full-thickness skin defect site of nude mice can accelerate wound

closure, reduce inflammation and improve wound healing quality. Overall, the DLP-printed dermal scaffold presents an appealing approach for effectively treating full-thickness skin defects in a clinical setting.

Keywords: 3D printing, dermal scaffold, photo-cross-linking, skin tissue regeneration.

Article Highlights

1. A bioink composed of methacrylated gelatin (GelMA) and chito-oligosaccharides (COS) has been developed for 3D printing dermal scaffolds loaded with HDFs to facilitate skin tissue regeneration.
2. The GelMA/COS composite bioink exhibits excellent biocompatibility and antibacterial activity, simultaneously reducing the expression of fibrosis-associated genes, including collagen I, collagen III, and fibronectin I.
3. The DLP-printed dermal scaffold demonstrated the ability to secrete characteristic extracellular matrix (ECM) proteins of the dermis, including collagen I, collagen III, and fibronectin I. In vivo experiments further indicated that the cell-laden scaffold can reduce inflammatory reactions and enhance wound healing quality.

1. Introduction

The skin functions as the primary defense against external environmental damage and prevents the invasion of microorganisms [1]. While most skin injuries can repair rapidly, extensive damage to the skin poses a complex wound healing process that cannot achieve self-repair [2]. This can lead to systemic issues, including bacterial infections and compromised immune system [3]. Additionally, skin wound repair primarily requires the regeneration of the dermis and skin appendages, including collagen fibers, elastic fibers and glycosaminoglycans, while also involving a multitude of cutaneous appendages such as blood vessels, hair follicles and sweat glands [4, 5]. However, unlike the epidermis, the dermis lacks comparable regenerative potential. Consequently, damaged dermal tissue tends to be replaced by scar tissue, necessitating specific interventions to promote healing [6]. In recent years, various tissue-engineered skin substitutes, including films, hydrogels, nanofiber membranes, and commercial skin substitutes, have been employed to accelerate wound healing [7-10]. Nevertheless,

these products are unable to fully replicate the microenvironment of healthy skin, leading to disparities in the morphology and functionality of the skin tissue [5]. 3D bioprinting technology can deposit biomaterials and cells layer by layer at specific locations, allowing for the construction of complex three-dimensional architectures and offering a promising opportunity for customized skin model fabrication [11, 12]. Currently, extrusion-based bioprinting is a widely used printing method [13]. However, achieving high printing resolution often requires sacrificing cellular viability to obtain high shear stress. Additionally, the range of printable viscosities is also limited [14, 15]. DLP is a photopolymerization printing technique that converts photosensitive liquid into a hydrogel structure [16]. Compared to extrusion-based printing, DLP printing offers advantages such as high cellular viability, high resolution, and fast printing speed [17]. Therefore, DLP printing holds the potential to mimic the precise spatial structure of natural tissues and achieve the reproduction of native dermal architecture.

The key to DLP printing lies in photopolymerizable hydrogels. Various photopolymerizable hydrogels have been developed for DLP-based 3D printing, such as Gelatin Methacrylate (GelMA), Photocurable Chitosan (CHIMA) and Poly (ethylene glycol) diacrylate (PEGDA) [18-20]. GelMA-based bioink, derived from collagen modification, has emerged as one of the popular bioinks in the field of 3D printing due to its excellent biocompatibility, on-demand photocuring properties, and adjustable physicochemical characteristics [21]. Shie et al. utilized varied GelMA concentrations to fabricate 3D-printed scaffolds with human dermal fibroblasts. Their investigation revealed that lower GelMA concentrations showed reduced printing resolution and limited shaping capabilities, yet promoted fibroblast proliferation and migration within a sparser microenvironment. Conversely, higher GelMA concentrations hindered cell diffusion and proliferation due to increased network density and stiffness [22]. Additionally, Rita et al. discovered that GelMA stiffness being too high could promote the activation of myofibroblasts by increasing the expression of fibrosis-related genes and proteins, leading to the formation of scar tissue [23]. Consequently, there is an urgent need for the development of a biomaterial with excellent printability and good biocompatibility for DLP-based 3D printing.

COS is derived from the hydrolysis of chitin or chitosan and has a relatively low molecular weight (MW < 3.9 kDa) [24]. It retains the antibacterial, anti-inflammatory, and excellent biocompatibility properties of chitosan while improving its water solubility, making it highly regarded in the field of tissue engineering [25-27]. Oh et al. employed a COS-salicylic acid conjugate to enhance the wound healing capabilities of alginate-gelatin hydrogels, resulting in increased collagen deposition and accelerated wound healing [28]. Furthermore, the antibacterial activity of COS plays a vital role in reducing bacterial infections and aiding tissue repair, particularly during the susceptible early stages of wound healing. Park et al. utilized COS as a substitute antibacterial material in order to enhance the antibacterial effectiveness of polyvinyl alcohol hydrogels for acne treatment, replacing conventional antibiotics [29, 30]. P. Chandika et al. had proven that COS with a molecular weight in the range of 1-3kDa exhibits the best cytocompatibility and has good application potential in wound healing [31]. As a result, we had opted for COS with a molecular weight less than 2 kDa to enhance the biocompatibility of high-concentration GelMA.

In this study, a composite bioink comprising GelMA and COS was developed for 3D printing of a dermal scaffold based on DLP technology (Fig. 1). The bioink formulation incorporated lithium phenyl-2, 4, 6-trimethyl benzoyl phosphinate (LAP) as the polymerization initiator. The physicochemical properties of the GelMA/COS bioink were evaluated through comprehensive assessments, including swelling, mechanical strength, degradation, and antibacterial activity. To ensure its suitability for skin tissue engineering, the bioink's biocompatibility was examined by HDFs, with attention given to the expression of ECM proteins and genes. Subsequently, the suitable GelMA/COS bioink was chosen for loading HDFs and fabricating a mesh-like dermal structure, resembling the native tissue, and the regenerative effects were studied through in vitro cultivation. Ultimately, a mouse model with full-thickness skin defects was developed to assess the effectiveness and mechanisms of the dermal scaffold in fostering wound regeneration.

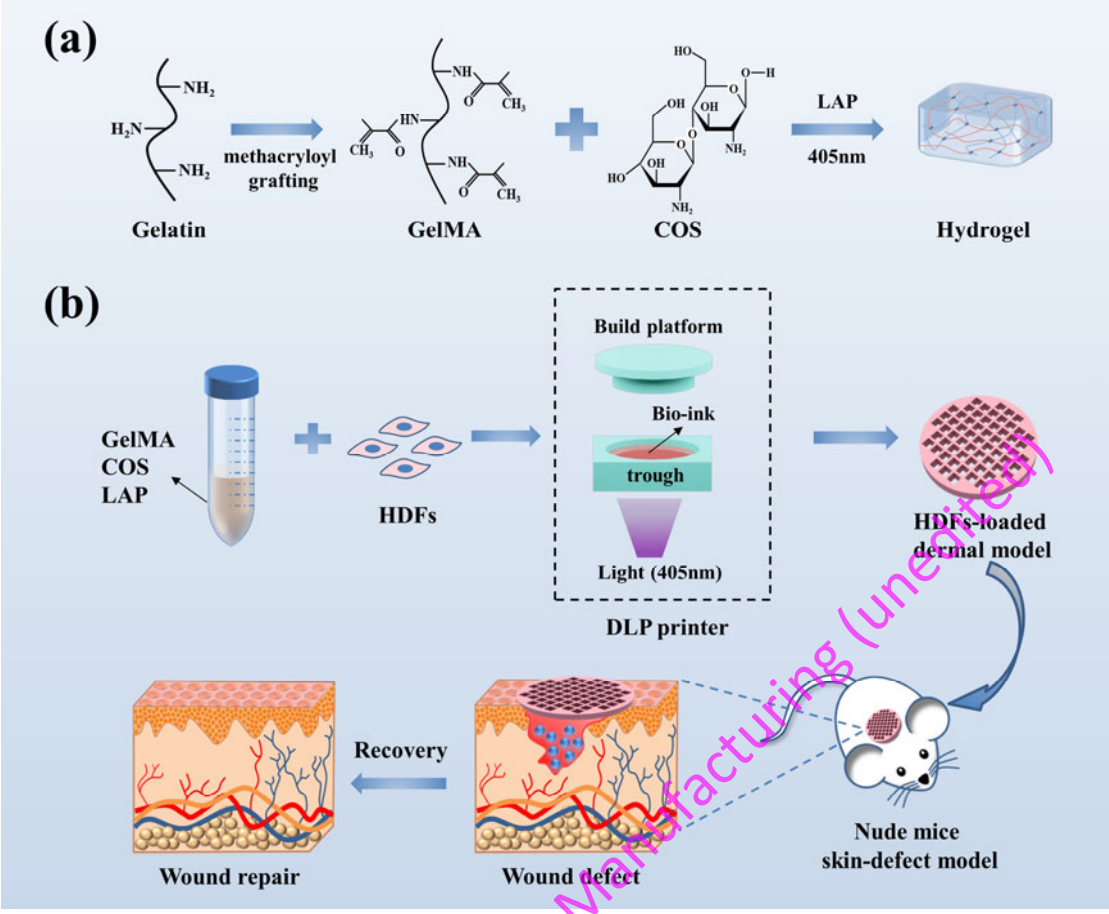

Fig.1 (a) Composition of GelMA/COS bioink and schematic diagram of hydrogel formation; **(b)** 3D bioprinted dermal scaffold and its application in full-thickness skin regeneration.

2. Materials and methods

2.1. materials

Chitosan oligosaccharides (COS, MW≤2000), gelatin, Methacrylic anhydride (MA), Dimethyl sulfoxide (DMSO) and Sodium hydroxide (NaOH) were purchased from Macklin (Shanghai, China). Lithium phenyl-2, 4, 6-trimethyl benzoyl phosphinate (LAP) was provided by StemEasy (Jiangsu, China). Human dermal fibroblasts (HDFs) were provided by BFB Company (Shanghai, China). Fetal bovine serum (FBS) was purchased from Gibco (Rockville, MD, USA). Dulbecco's modified Eagle's medium (DMEM) was provided by Cytiva (USA). Phosphate buffer saline (PBS), Live/dead assay kit, Phalloidin, 4,6-diamidino-2-phenylindole (DAPI) and cell counting kit-8 (CCK-8) were provided by BestBio (Shanghai, China). LB Broth, Plate Count Agar (PCA) and Penicillin-Streptomycin-Gentamicin Solution, 100× were purchased from Solarbio (Beijing, China). The Staphylococcus aureus (S. aureus) and Escherichia coli

(E. coli) were purchased from Biobw (Beijing, China). Hematoxylin-eosin (HE), Masson's Trichrome Stain Kit, Single-use SABC-POD (Mouse/Rabbit IgG) assay kit, human anti-COL1A1, COL3A1 and FN1 antibodies, and mouse anti-CK10, CK14, CD31 and α-SMA antibodies were provided by BOSTER (Wuhan, China). The chemicals and reagents used in the research were all analytical grade.

2.2. Synthesis of GelMA

GelMA was accomplished in accordance to the process in a former research study [22]. In summary, 10g gelatin was dissolved in 100 mL PBS at 50 ℃ to obtain 10% w/v gelatin solutions. Then, 500 μL methacrylic anhydride was dripped into the gelatin solution at a rate of 0.5 mL/min, while being continually stirred for 2 h to allow modification. Then, 400 mL warm PBS was added into the gelatin-methacryloyl solution, followed by a stirring period of 10 minutes to terminate the reaction. The resulting solution dialyzed in ultrapure water for 7 days at 40 ℃ and then centrifuged to remove any excess unreacted substances. The dry GelMA foam was obtained by lyophilization and stored at -20 ℃.

2.3. DLP 3D printing of GelMA/COS hydrogels

The bioink was composed of GelMA, various concentrations of COS and LAP. GelMA foams and LAP were dissolved in PBS solution at a temperature of 50 ℃, with respective concentrations of 10% (w/v) and 0.3% (w/v). Subsequently, various quantities of COS were added to obtain the final GelMA-COS concentration of 10%-0% (G10C0), 10%-1% (G10C1), 10%-3% (G10C3), 10%-6% (G10C6) (w/v). The mixed solution underwent vortexing and was subsequently incubated at a temperature of 50 ℃ until clarification was achieved. Once clarified, the solution was sterilized using a 0.22 μm filter through filtration.

A DLP-based 3D printer was employed to fabricate GelMA/COS hydrogels. The prepared solution was subsequently transferred to the material tank positioned beneath the construction platform, to which the cured hydrogel can be attached. The pre-designed 3D model was imported in the computer, and the Creation Workshop software was used to slice the model and set the printing parameters, then control the vertical movement of the platform and image to the projector to start printing. During printing,

The GelMA/COS solution was irradiated with 405 nm blue light at 10 mW/cm² for 15-30 s with a layer thickness of 50 μm. Finally, the prepared hydrogel was detached from the construction platform and subsequently immersed in deionized water to eliminate residual impurities prior to further measurements.

2.4. Characterization of the GelMA/COS hydrogels

2.4.1 Chemical analysis by FTIR

The Infrared absorption spectra of GelMA/COS hydrogels were identified utilizing Fourier transform infrared spectroscopy (FTIR TENSOR 27, Germany). The process of measurement took place in room temperature conditions, scanning frequencies from 400 to 4000 cm^{-1} at a 4 cm^{-1} resolution. Before measurement, all samples were subjected to freeze-drying and then pulverized into a powder form.

2.4.2 Water uptake capacity and degradation tests

For water uptake capacity, the samples were printed into cylinders, each boasting a diameter of 10 mm and standing 7 mm tall. Prior to the measurement, the hydrogels were lyophilized to remove any residual moisture. Subsequently, the dried hydrogels were soaked in deionized water and weighed at different time intervals to track any changes in weight. The quantification of the water uptake capacity (C_w) for the samples was computed using the following formula:

$$C_w = (W_t - W_0) / W_0 \times 100\%$$

where W_t represented the mass of the samples soaked at different time and W_0 corresponded to initial weight of lyophilized samples.

For degradation test, the printed hydrogels were soaked in PBS for 24 h to achieve swelling equilibrium. Afterward, any excess water on the hydrogels surface was gently wiped off with a filter paper and weighed (W_0). The samples were then placed in a PBS solution containing type II collagenase (2 U/mL) at 37 ℃ for two weeks. The collagenase solution was changed once on two days, the hydrogels were dried and weighed (W_i) at different time points. The calculation for the remaining weight percentage was carried out with the given formula:

$$\text{Remaining weight (\%)} = W_i / W_0 \times 100\%$$

2.4.3 Measurement of mechanical properties

An Instron 3343 (Instron Instruments, USA) was used at room temperature to characterize the mechanical properties of the hydrogels. Initially, cylindrical samples with 10 mm diameter and 7 mm height were printed. The compression test is conducted at the compression speed of 0.6 mm/min. Next, the slope of the stress-strain curve's linear region, within a strain range of 10% to 20%, was calculated to determine the compression modulus.

2.4.4 Morphological analysis

A scanning electron microscope (SEM, SU8010-HITACHI, Japan) was used to investigate the morphological features of the hydrogels. The cylindrical hydrogels were subjected to lyophilization, then sliced, and the sections were sprayed with gold for interior microstructure observation. Analysis of both the porosity and pore size was conducted using Image J software (National Institute of Health, USA).

2.4.5 Antibacterial tests

The Staphylococcus aureus (S. aureus, CMCC26003) and Escherichia coli (E. coli, ATCC8739) were used as the typical bacteria of gram-positive and gram-negative bacteria, respectively. Before use, both bacteria underwent an overnight culture in LB medium at a temperature of 37 ℃ and a speed of 150 r/min.

The plate colony counting method was utilized to identify the level of antibacterial resistance that various samples had towards S. aureus and E. coli [32]. Briefly, the hydrogel samples were made into discs and placed in 24-well plates, then the cultured bacterial solution was diluted to 10^6 CFU/mL with sterilized PBS and 10ul of bacterial suspension was added to the hydrogel surface. Following a 6 h incubation period in a 37 ℃ environment, each well had 1ml of sterile PBS added to enable the bacterial re-suspension. Then 100ul of bacterial suspension was added stepwise to the prepared agar plate medium, spread evenly with coated rods and incubated in a 37 ℃ incubator for 24 h. Finally, photographs of the agar plates were taken of, and the count of colony-forming units (CFU) was ascertained utilizing Image J. The antibacterial ratio was computed based on the subsequent formula:

$$\text{Antibacterial ratio (\%)} = (CFU_{control} - CFU_{experiment}) / CFU_{control} \times 100\%$$

where the G10C0 group was designated as the control, other groups were designated as the experiment.

2.5. Cytocompatibility study of hydrogels in vitro

2.5.1 Cell culture and viability

HDFs were grown in DMEM enhanced with 10% FBS and 1% penicillin-streptomycin-amphotericin B. The culture was maintained at 37 ℃ in a humidified environment composed of 5% CO_2. Every two days, the culture medium was exchanged, and once the cell confluence exceeded 80% in the flask, the cells were passaged and utilized for cytocompatibility assays.

After culturing for 1, 4, and 7 days, a live/dead assay kit was utilized to evaluate cell viability through staining. Briefly, each sample was individually submerged in PBS infused with Calcein-AM and propidium iodide (PI), followed by incubation at 37 ℃ for a determined period. The stained samples were then observed under a fluorescence microscope (BZ-X800LE, KEYENCE, China).

2.5.2 Cell proliferation

Cell proliferation in various hydrogels was assessed on day 1, 4, and 7 using the CCK-8 kit. The medium in the samples was removed and the samples were rinsed twice with PBS. Following this, each well was treated with 50 μL of CCK-8 working solution and 450 μL of DMEM. After one hour of incubation at 37 ℃, 100 μL of the samples were aspirated and moved to a 96-well plate. Finally, a microplate reader (BIORAD) was utilized to measure the absorbance at 450 nm. Triplicate testing was executed for each sample group.

2.5.3 Cell morphology

The cellular morphology within the hydrogels was studied using DAPI and phalloidin staining after 7 days cultivation. Briefly, the specimens underwent three rounds of washing with PBS before being fixed with 4% paraformaldehyde at 4 ℃ for half an hour. Subsequently, membrane was permeabilized for 10 minutes at room temperature with 0.1% Triton-X 100. And the samples underwent a 1 h incubation in

PBS enriched with 1% BSA, before being subjected to phalloidin and DAPI staining in the dark for 45 and 20 minutes respectively. Ultimately, the cells' cytoskeletons and nuclei were visualized using a fluorescence microscope.

2.5.4 Immunofluorescence staining

After 7, 14 days of culture, immunofluorescence staining was performed to analyze COL1A1, COL3A1 and FN1 expression in the different hydrogels. The samples were treated with 4% paraformaldehyde for a 30 min fixation, and then were permeabilized for a duration of 10 minutes using 0.1% Triton-X 100. This was followed by a 1-hour blocking procedure using goat serum. Subsequently, the hydrogels were then incubated respectively with primary antibody against COL1A1 (BA0325,1:200) and COL3A1 (M00788-1, 1:100) and FN1 (BM4460, 1:50) at 4 °C overnight. Next, they were treated with a secondary antibody sheep anti-rabbit IgG (1:100) for 1 h, and stained with DAPI for 15 min, all carried out in a light-avoidance environment. Finally, the samples were photographed and analyzed by a fluorescence microscope.

2.5.5 RT-PCR

The expression of genes involved in wound regeneration after 7 and 14 days of culture was evaluated using RT-PCR, as previously reported [23]. Briefly, the cultured samples were incubated in PBS containing 2 mg/ml type II collagenase for a duration of 30 minutes. Subsequently, cells were collected through centrifugation, followed by the isolation of total RNA using Trizol reagent (Invitrogen). After dissolving the extracted RNA in enzyme-free water, its concentration was quantified with the aid of a spectrophotometer (NanoDrop OneC, Thermo Scientific). Subsequently, the isolated RNA was reverse-transcribed using PrimeScript^{TM} RT Master Mix to generate the cDNA. The obtained cDNA was combined with the primer pair of COL1A1, COL3A1 and FN1, glyceraldehyde-3-phosphate dehydrogenase (GAPDH) was employed as the reference gene. Then, a 7900 real-time PCR system (Applied Biosystems) was utilized to perform quantitative real-time polymerase chain reaction (PCR). The PCR primer sequences are shown in Table 1.

Table 1. Primer sequence used in RT-PCR

Gene	Primer sequence (5'→3')
Collagen I (COL1A1)	F: AAAGATGGACTCAACGGTCTC
	R: CATCGTGAGCCTTCTCTTGAG
Collagen III (COL3A1)	F: CTCAGGGTGTCAAGGGTGAAAGTG
	R: TGTACCAGCCAGACCAGGAAGAC
Fibronectin I (FN1)	F: AATAGATGCAACGATCAGGACA
	R: GCAGGTTTCCTCGATTATCCTT
GAPDH	F: GCCACATCGCTCAGACACC
	R: CCCAATACGACCAAATCCGT

2.5.6 3D-printed dermal scaffold

When the cell confluence was 80%, HDFs were uniformly suspended in sterile bioink (1×10^6 cells/mL) that had been produced with G10C1 for printing. The created bioink was then moved to the material tank, where the 10 mm diameter and 1 mm height dermal grid structure was printed after the DLP device had been installed in a sterile environment. Printing parameters were used as follows: line width: 300 μm, pore size: 700 μm, layer thickness: 50 μm, blue light irradiation time: 10 s, light intensity: 12 mW/cm^2. After printing, the printed dermal scaffold was immersed in DMEM to remove the unreacted solution, after which it was placed into DMEM with 10% FBS and 1% penicillin-streptomycin-amphotericin B. This scaffold was subsequently incubated in a humid atmosphere with a consistent temperature of 37 ℃ and a CO_2 concentration of 5%.

2.6 In vivo implantation experiment

2.6.1 Full-thickness skin defect model on the back of nude mice

The approved guidelines of the Animal Ethics Committee at the First Hospital of Shanxi Medical University were followed for all animal experiments conducted. To evaluate the efficacy of the printed dermal scaffold in promoting wound regeneration, full-thickness skin wounds were created on the nude mice's dorsal surface. Male nude mice, aged between 4-6 weeks and weighing 20-25 grams, were arbitrarily distributed into control, hydrogel, and cell-laden scaffold groups. For the "hydrogel" group, no cells were mixed in bioink to print into a disk-shaped hydrogel. Mice were anesthetized with 2% isoflurane before surgery and a full-thickness circular skin wound with a 10

mm diameter was inflicted on their backs. Then the cultured hydrogel and cell-laden scaffold were implanted into the wound, and both sides of the wound were sutured to prevent the scaffold from falling off. Finally, the wound was covered with a commercially available wound dressing (Tegaderm Film, 3m, MN). Digital photographs were captured on different days (0, 3, 7, 10, and 14) to document the progression of the wound healing process. The wound area in the photographs was then quantified using Image J software.

2.6.2 Histologic and immunostaining analysis

At 7, 14, and 21 days after transplantation, mice were euthanized, and full-thickness wound tissue was gathered, followed by fixation in 4% paraformaldehyde for a duration of 24 hours. Then the samples were encased in paraffin and were cut into sections 5 μm thick using a paraffin tissue slicer (Leica RM2245). These sections underwent staining with haematoxylin and eosin (H&E), along with Masson's trichrome (MT), intended for histological examination. For immunohistochemistry staining, the sections underwent dewaxing in xylene, gradient hydration in ethanol, and rinsing in PBS. Furthermore, these sections were also treated with a 3% hydrogen peroxide solution for a duration of 10 minutes to eliminate endogenous catalase. They were subsequently digested in composite digest for 30 min at 37 ℃ to achieve antigen repair and then inhibited with a 5% BSA solution for another 30 minutes. Then, they were incubated with the anti-murine primary antibodies CK10 (BM4422, 1:100), CK14 (A01432, 1:200), TNF-α (A0277, 1:100)，CD31 (A01513-3, 1:200) and α-SMA (BM3902, 1:100) at 4 ℃ overnight. Subsequently, the sections were allowed to equilibrate at room temperature for 30 min and incubated with biotin-labeled goat anti-rabbit/mouse IgG and SABC at 37 ℃ for 30 min. Finally, the sections were developed with DAB chromogen for 2 min, stained with hematoxylin for 1 min and covered with neutral resin. All stained sections were scanned using Panoramic MIDI digital slide scanner (3DHISTECH, Budapest, Hungary).

2.7 Statistical analysis

GraphPad Prism 5 software was used for statistical analysis, and one-way analysis of variance (ANOVA) with Tukey's test were employed to identify group differences.

ns ⩾ 0.5, *p < 0.05, **p < 0.01, and ***p < 0.001 was considered statistically significant. All data results were presented as mean ± standard deviation (SD).

3. Results and discussion

3.1 Preparation and characterization of GelMA/COS hydrogels

COS exhibits desirable properties such as water solubility, absorption capacity, biocompatibility, and antimicrobial activity [33]. Nonetheless, the direct application of COS in skin regeneration is hindered due to its low molecular weight [30]. GelMA is an optically curable hydrogel that can create a favorable environment for implanted cells, promoting their proliferation and differentiation [22]. In this research, we endeavored to develop a highly biocompatible photo-cross-linked bioink by copolymerizing COS (MW⩽2000) alongside GelMA. Subsequently, this novel bioink was employed for the 3D bioprinting of dermal structures within the skin context.

Fourier transform infrared (FTIR) spectroscopy was used to confirm the composition of the hydrogel and to study any changes in the chemical structure after soaking in deionized water for 14 days (Fig. 2a). Specifically, in GelMA, the FTIR spectrum shows peaks at 1238 cm^{-1} and 1630 cm^{-1}, which represent the N-H bonds of amide III and the C=O stretching in amide I, respectively. Additionally, the peaks at 3061 cm^{-1} and 3260 cm^{-1} correspond to the C-H stretching of amide B and the N-H stretching of amide A, respectively. These results provided confirmation that GelMA possessed the required chemical structure [34]. In COS, the N-H bending of amide II was represented by the peak at 1512 cm^{-1}, while the peaks at 1150 cm^{-1} and 1036 cm^{-1} were attributed to the characteristic asymmetric stretching of C-O-C and stretching of C-O, respectively [35, 36]. The FTIR spectra for the GelMA/COS hydrogel showed similar characteristic peaks to that of GelMA, with no additional peaks. However, the intensity of the C-O stretching peak in COS increased with increasing COS concentration, indicating the successful fabrication of GelMA/COS hydrogel. Fig. S1 investigated the effect of COS concentration on the gelation time of photocurable GelMA hydrogel using the inverted gelation method. The gelation time was defined as the point at which the solution stopped flowing [37]. The experimental findings

indicated a positive correlation between the concentration of COS and the gelation time, as an increase in the COS concentration led to a gradual prolongation in gelation time, ranging from 10 s to 30 s. This phenomenon can be ascribed to the introduction of COS, which induces partial disruption of GelMA's crosslinking structure, consequently inducing a decelerated advancement of the photocuring reaction process. Subsequently, in vitro analysis of the hydrogel's characteristics was performed to determine the ideal concentration for producing a dermal scaffold that mimics the properties of the skin's dermal tissue.

First, the water absorption capacity of hydrogels plays a crucial role in expediting wound healing by effectively absorbing wound exudates and reducing the risk of infection [2]. Additionally, it serves as a vital parameter in ensuring the structural wholeness and dimensional stability of scaffolds throughout in vitro cell cultivation and in vivo implantation [38]. Experimental findings revealed that all hydrogels achieve equilibrium water uptake within a span of 2 days (Fig. 2b), exhibiting a water uptake range of 500% to 670%. Among them, G10C6 exhibited the highest water uptake capacity, measuring approximately 660%. The extent of water uptake escalated in proportion to the increase in COS concentration. This occurrence can be ascribed to the reality that the elevated COS content diminishes the cross-linking density of GelMA and potentially leads to a part of COS solubilization in water, thereby enhancing the water uptake capacity of the hydrogel [39]. Due to the inherent presence of hydrophilic groups in natural polymers like gelatin and chitosan, GelMA/COS hydrogels exhibit remarkable hydrophilicity. This is evident in the representative images and contact angles shown in Fig. S2, respectively. Among them, the G10C6 hydrogel demonstrated the strongest hydrophilicity with a contact angle of 29.4°. This suggested that the hydrophilicity of the hydrogel was further enhanced after the addition of COS to GelMA, which was advantageous for cell adhesion and proliferation.

Hydrogels should possess the inherent capability to degrade in the presence of natural enzymes, as this attribute is a critical indicator when assessing the scaffold's potential to support the formation of new tissue [40]. Therefore, the physical and chemical stability of the scaffold was assessed through in vitro collagenase degradation

experiments. Fig. 2c showed that incorporating COS into the hydrogel formulation enhances its rate of degradation. By the seventh day, GelMA retained 60% of its initial mass. However, as the concentration of COS increased, the remaining masses decreased to 32%, 23%, and 10%, respectively, indicating a faster degradation rate. This can be attributed to the observed decrease in the crosslinking density of GelMA, as confirmed by FTIR and swelling analysis.

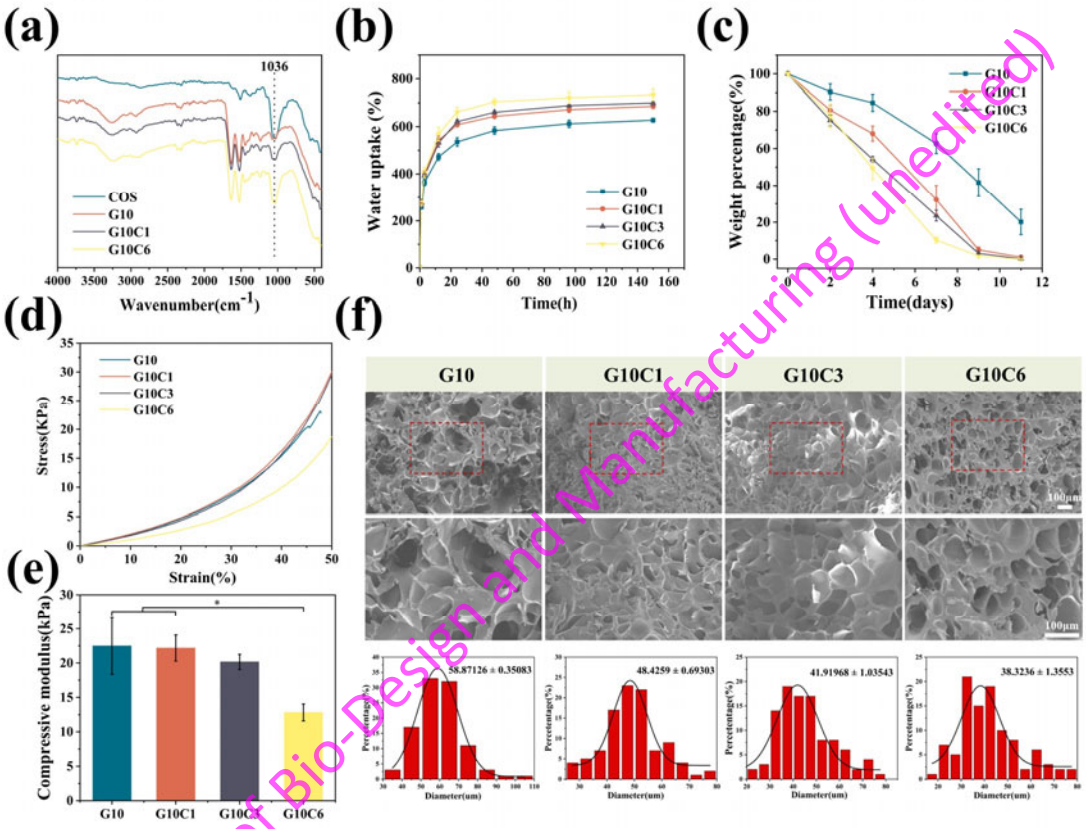

Fig. 2 Materials characterization of GelMA/COS hydrogels. **(a)** FTIR spectra of pure COS, GelMA, and different ratios of GelMA/COS; **(b)** Swelling degree of hydrogels after 6 days of incubation; **(c)** Degradation curve in collagenase; **(d)** Stress-strain curve; **(e)** Compressive modulus; **(f)** Cross-sectional SEM images and pore size distribution of hydrogels. For statistical significance: *p < 0.05, **p < 0.01 and ***p < 0.001.

In order to assess the mechanical adaptability, the compressive stress−strain curves of photocurable hydrogels were obtained (Fig. 2d). The results described its resistance to deformation under initial pressure, subsequent stiffening with increased strain, and eventual fracturing [41]. G10 hydrogel fractured within a strain range of 47%. However, the introduction of COS enhanced the fracture strain of the hydrogels, indicating

improved elasticity [42]. The compression modulus, derived from the stress-strain curve, revealed a gradual decrease in the hydrogel's modulus from 27±0.06 kPa to 13±0.04 kPa with increasing COS concentration (Fig. 2e). These findings align with the earlier analysis, suggesting that the disruption of the cross-linked structure of GelMA hydrogel leads to a decline in its mechanical properties.

Besides, the porous structure within hydrogels assumes a pivotal role in facilitating cell adhesion and migration, as well as promoting the exchange of oxygen and nutrients, and removing metabolic waste products [43]. In our research, analysis of scanning electron microscopy (SEM) images revealed a porous and interconnected microstructure present on the cross-sections of all scaffolds. Notably, as the concentration of COS increased, a gradual reduction in pore size within the hydrogel was observed. Specifically, the pore size of G10 was 58.9±0.35 μm, G10C1 was 48.4±0.69 μm, G10C3 was 41.9±0.14 μm, and G10C6 was 38.3±1.36 μm (Fig. 2f). The addition of COS increased the porosity of the support, from 52.91% to 77.07% (Fig. S3). The decrease in pore size and increase in porosity were mainly attributed to the low molecular weight of COS [31].

3.2 In vitro antibacterial activity of GelMA/COS hydrogels

The presence of bacterial infection can obstruct the wound's natural healing progression, thus prolonging the closure time of the wound. It is a dominant factor leading to the development of post-surgical complications in numerous patients [44]. In this study, surface antibacterial experiments were conducted to evaluate the antibacterial activity of COS against E. coli and S. aureus.

The bacterial colonies shown in Fig. 3a were noted on the agar plates after incubation for 24 hours at 37 °C, using the G10 group as a reference. The inhibitory rates of G10C1, G10C3, and G10C6 against S. aureus were 79%, 90%, and 94%, respectively, while against E. coli, the inhibitory rates are 83%, 90%, and 95%, respectively (Fig. 3b, c). These findings indicated that as the concentration of COS increases, the antibacterial activity of the hydrogel gradually strengthens. This was primarily due to the binding of positively charged amino groups on COS with negatively charged groups on the microbial surface. This interaction leads to the

damage of bacterial cell membranes in turn enhancing their permeability. Consequently, the positively charged groups can more easily penetrate the bacterial cells, thereby influencing their normal proliferation behavior and achieving an effective bacteriostatic effect [45]. Additionally, when the COS concentration was 1%, the inhibitory rate against E. coli surpassed that against S. aureus, demonstrating that gram-negative bacteria exhibited greater sensitivity to low-molecular-weight COS. This outcome aligned with previous research in the field [46].

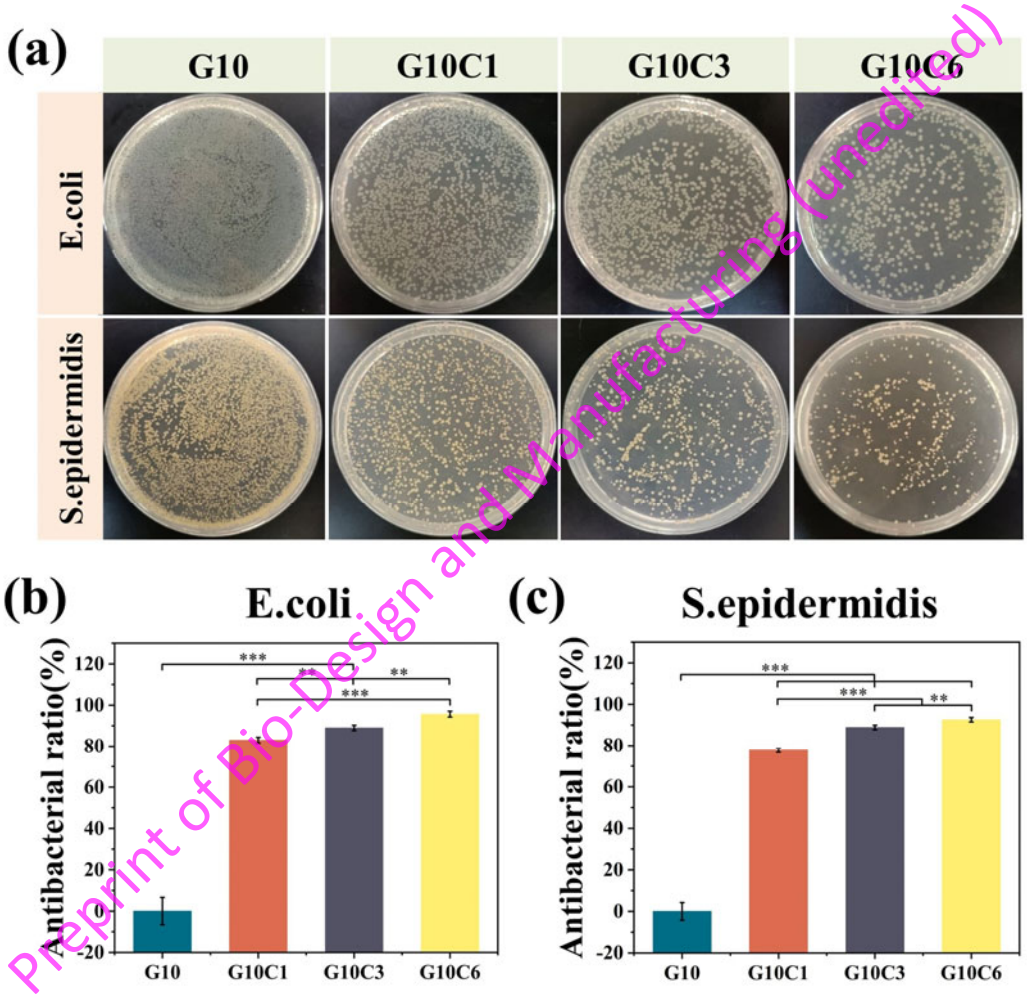

Fig. 3 In vitro antibacterial performance of the GelMA/COS hydrogels. **(a)** Image of bacterial colony forming units on the hydrogel after 6 hours of culture; Antibacterial ratio against **(b)** E. coli and **(c)** S. aureus. For statistical significance: *p < 0.05, **p < 0.01 and ***p < 0.001.

3.3 In vitro biocompatibility of GelMA/COS hydrogels

In order to investigate its role in skin regeneration, this study aimed to assess the biocompatibility of HDFs-laden photocurable hydrogels by evaluating cell proliferation, cell viability, and cell morphology. Firstly, CCK-8 experiment was conducted to

measure cell proliferation. The results (Fig. 4a) demonstrated that after 7 days of incubation, HDFs within all hydrogels showed proliferation, with an enhanced proliferative capacity observed as the concentration of COS increased. This indicated that the inclusion of an appropriate amount of COS can promote HDFs proliferation. Subsequently, live/dead staining experiment (Fig. 4b) was conducted to evaluate cell viability, revealing a higher cell viability in all hydrogels with prolonged culture time. Additionally, the morphology of HDFs within the hydrogels was examined using FITC-phalloidin and DAPI staining on day 7 (Fig. 4c). The cells exhibited satisfactory growth, predominantly displaying a round shape. This may be attributed to the confinement effect exerted by the hydrogel matrix, which constrained HDFs spreading.

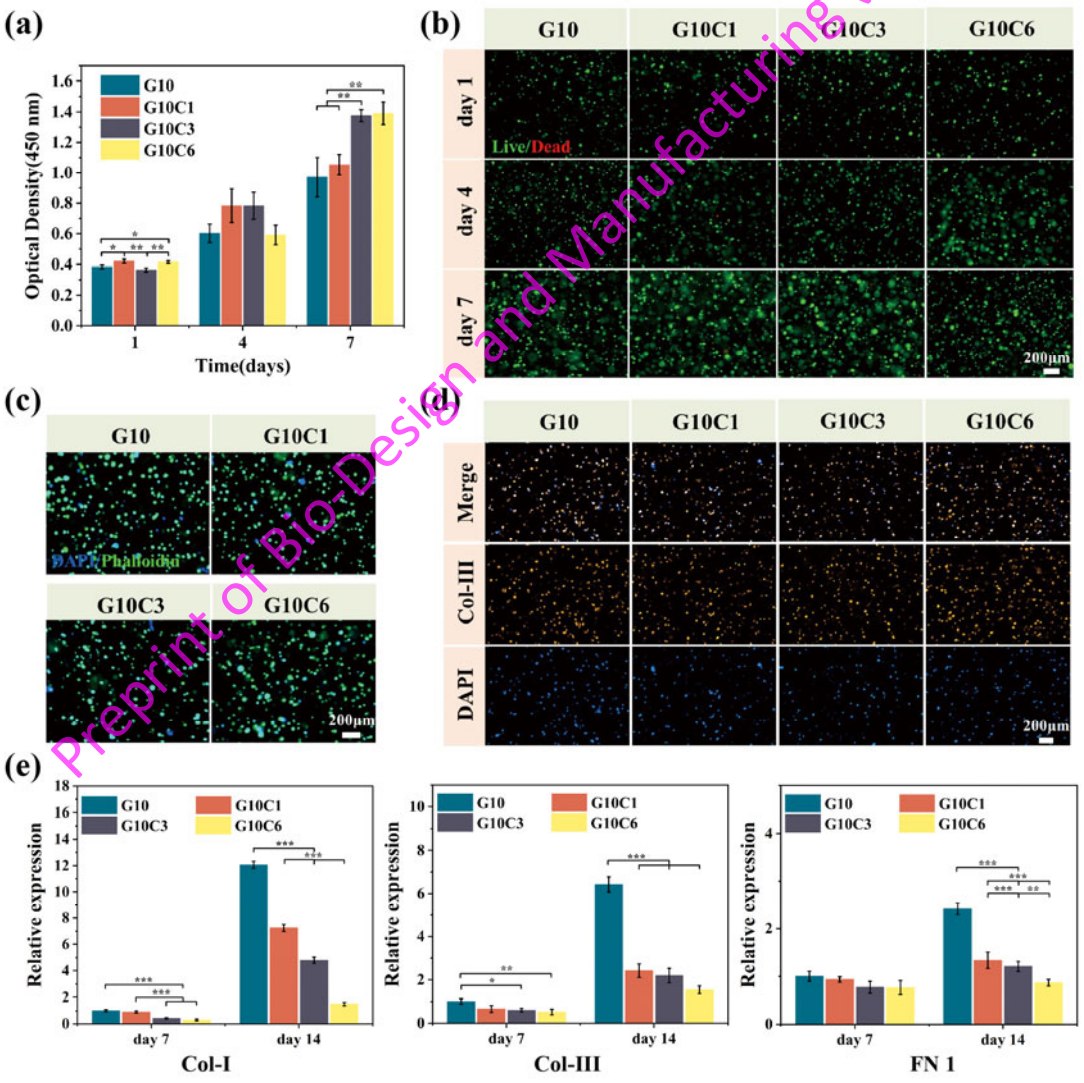

Fig. 4 Biocompatibility assessment of GelMA/COS hydrogels loaded with HDFs. **(a)** Cell proliferation evaluation of HDFs at 1, 4, and 7 days of culture; **(b)** Live/dead staining images

of HDFs at days 1, 4, and 7 (green: live cells, red: dead cells), Scale bar: 200 μm; **(c)** Immunofluorescence images of HDFs at day 7 stained for Phalloidin/DAPI (green: actin filaments, blue: cell nucleus), Scale bar: 200 μm; **(d)** Immunofluorescence images of Col III deposition at day 14 of culture (red: Col III, blue: cell nucleus), Scale bar: 200 μm; **(e)** RT-PCR assessment of genes expression of Col I, Col III, and FN1 in HDFs cultured for 7 and 14 days. For statistical significance: *p < 0.05, **p < 0.01 and ***p < 0.001.

To further elucidate the regenerative capacity of the hydrogel to promoting skin tissue regeneration, the expression of Col-III protein was evaluated using immunofluorescence staining. Additionally, vital ECM gene expression levels, including Col-I, Col-III, and FN1, were carried out through real-time RT-PCR analysis (Fig. 4d, e). After 14 days of HDFs differentiation culture, immunofluorescence staining revealed uniform distribution of Col-III within all hydrogels (Fig. 4d), although it was difficult to discern differences between different hydrogel groups. RT-PCR analysis (Fig. 4e) demonstrated the impact of the internal microenvironment of the four hydrogels on the expression of ECM genes. The results indicated that after 7-14 days of cultivation, the expression levels of Col-I, Col-III, and FN1 were upregulated in all groups. However, at day 14, the G10 group exhibited significantly higher expression levels of these genes compared to the other groups, potentially leading to excessive deposition of ECM proteins and scar formation [47]. Moreover, the addition of COS suppressed the expression of these fibrosis-related genes, with the inhibitory effect increasing as the concentration of COS increased, similar to chitosan [48]. To summarize, the G10C1 hydrogel exhibited favorable mechanical properties, swelling degree, degradation rate, and biocompatibility, making it well-suited for dermal scaffolds and facilitating the regeneration of skin tissue. As a result, G10C1 laden with HDFs was the chosen bioink for 3D printing dermal scaffolds and subsequent testing.

3.4 DLP-based 3D printing of cell-laden dermal scaffold

To investigate the feasibility of utilizing G10C1 as a bioink for 3D printing, a DLP printer was used to sequentially solidify and print a grid-like structure (Fig. 5a). The microscopic and SEM observations were employed to examine the cross-sectional microstructure of the dermal scaffold (Fig. 5b-d), and the results showed that the pores

in the prepared grid were uniformly distributed and interconnected. This structure can increase the contact area, promote cell migration, nutrient exchange, and the excretion of metabolic waste products [49]. Additionally, the scaffold has the ability to induce the differentiation of HDFs along the lines and promote the secretion of ECM proteins.

To evaluate the biocompatibility of DLP-printed dermal scaffolds, the scaffolds were stained using live/dead assay on days 0, 1, 4, and 7 (Fig. 5e). The staining results on day 0 indicated that the printing process had no adverse effects on the cells, and the cells were evenly distributed throughout the scaffold. After 7 days of culture, the cells exhibited healthy growth and proliferation. Further morphological changes of HDFs were observed on days 4 and 7 using FITC-phalloidin and DAPI staining (Fig. 5f). After 7 days, HDFs were observed to grow along the pores of the printed structure and underwent spindle-shaped differentiation. These results validated that the G10C1 bioink loaded with HDFs for DLP printing does not interfere with cell behavior and facilitates HDFs proliferation and differentiation. Additionally, immunofluorescent staining at 14 and 21 days demonstrated successful secretion of extracellular matrix proteins, including Col-I, Col-III, and FN1 by HDFs (Fig. 5g), indicating the potential of the dermal scaffold in promoting skin tissue regeneration.

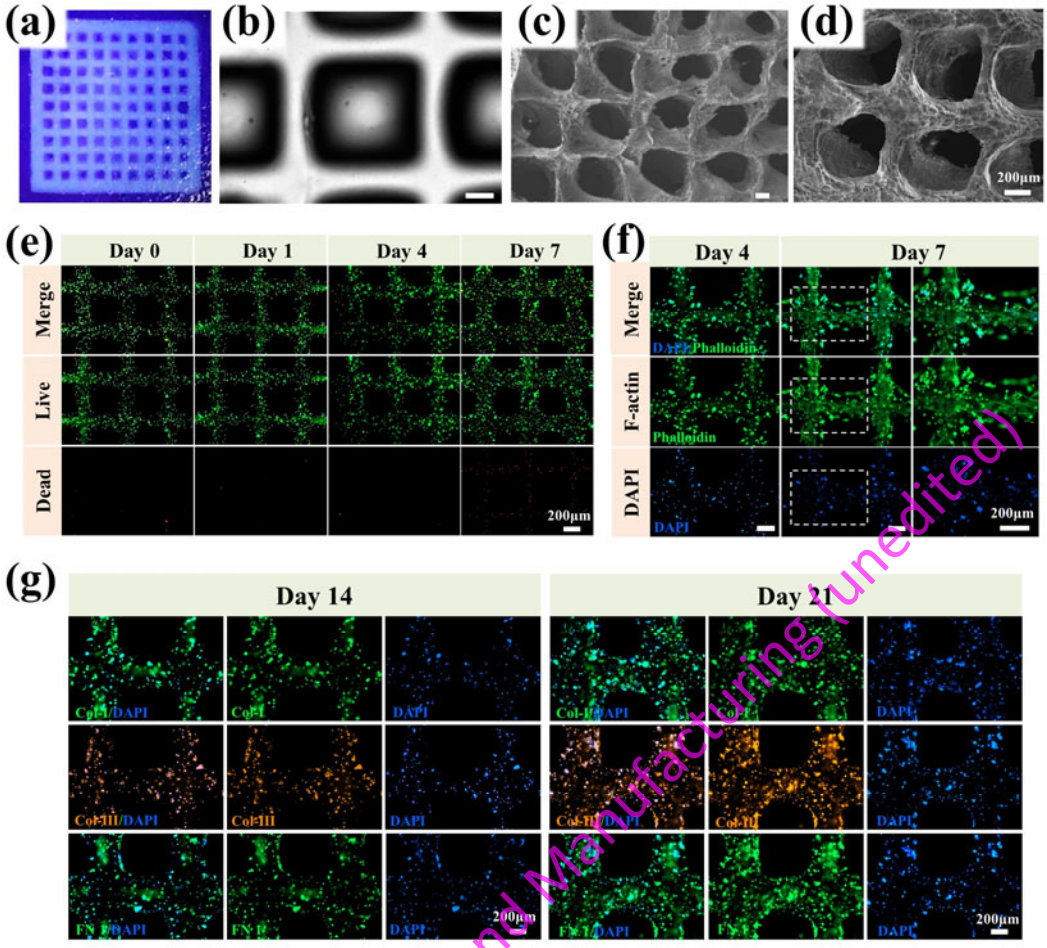

Fig. 5 Printability and biocompatibility assessment of 3D printed dermal scaffolds. **(a)** Digital photograph of the 3D printed grid-like structure; **(b)** Microscopic image of the grid-like structure, scale bar: 200 μm; **(c, d)** SEM images of the grid-like structure, scale bar: 200 μm; **(e)** Live/dead staining of HDFs-laden dermal scaffold after printing and at 1, 4, and 7 days of culture (green: live cells, red: dead cells), scale bar: 200 μm; **(f)** Immunofluorescence staining of Phalloidin/DAPI at 4 and 7 days of culture (green: actin filaments, blue: cell nucleus), scale bar: 200 μm; **(g)** Immunofluorescence staining of Col-I, Col-III, and FN1 at 14 and 21 days of culture (green: Col-I and FN1, red: Col-III, blue: cell nucleus), scale bar: 200 μm.

3.5 In vivo wound healing evaluation

A model of a full-thickness skin defect in nude mice was utilized to assess the effectiveness of dermal scaffold in enhancing wound healing. As shown in Fig. 6a, the wound healing process was observed at different time points for each group. The group with cell-laden scaffold showed the fastest wound contraction, the contour stacking results of the wound beds also indicated a higher promoting effect on wound healing

(Fig. 6b). At day 3, the cell-laden scaffold had a wound contraction rate of 66%, which was higher compared to the control group's rate of 19% and the hydrogel group's rate of 48% (Fig. 6c). The similar results were also obtained at day 7. After 14 days, it was observed that the wound in the control group had minimal remaining, while the other two groups showed almost complete closure. This mainly attributed to the synergistic effect of GelMA with COS to improve the wound healing rate by inhibiting the inflammatory response and the exchange of effective nutrients in grid-like structures [36, 49].

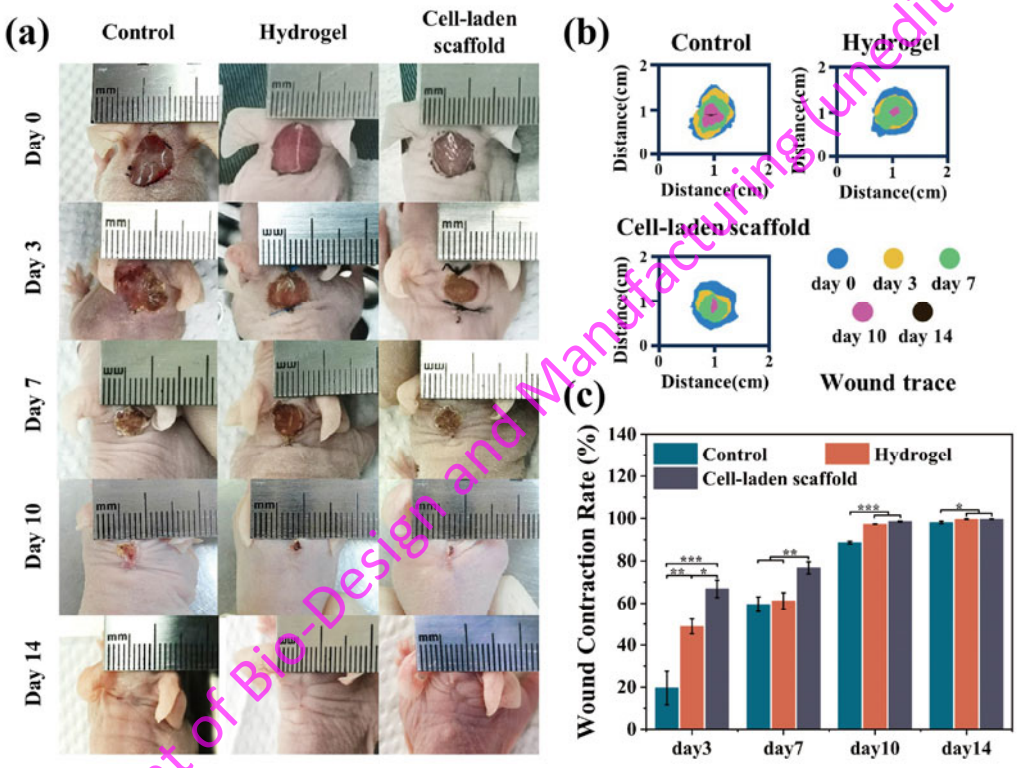

Fig. 6 3D-printed cell-laden dermal scaffolds for nude mouse full-thickness skin defect repair. **(a)** Representative photographs of the wound site at day 3, 7, 10, and 14 post-treatments with hydrogel and cell-laden scaffold respectively, the untreated group functioned as the control group; **(b)** Trajectory of wound bed closure within 14 days of treatment; **(c)** Wound contraction rate. For statistical significance: *$p < 0.05$, **$p < 0.01$ and ***$p < 0.001$.

In order to assess the quality of wound healing, histological analysis was used to further investigate inflammatory cell infiltration, fibroblast migration, granulation tissue development, and collagen deposition [50]. H&E staining results are shown in Fig. 7a, and the cell-laden scaffold group exhibited a narrower wound gap than the other

groups. At day 7, during the pre-wound healing period, it was observed that the hydrogel and cell-laden scaffold groups had fewer inflammatory cells compared to the control group. Additionally, an increased number of fibroblasts was observed, particularly in the cell-laden scaffold group. In addition, the thickness of the epidermal layer and the length of the wound are crucial factors in evaluating the effectiveness of wound healing [51]. According to the measurement results obtained from the Image J software, after 21 days, the cell-laden scaffold group exhibited a thickness of the epidermal layer similar to that of normal skin. In contrast, both the control group and hydrogel group displayed a much thicker epidermal layer (as shown in Fig. 7c). Furthermore, the length of the wound decreased over time (Fig. 7d). It was noteworthy that at day 14, the length of the wound in the cell-laden scaffold group was 1440.81 μm, shorter than the length of the wound in the control group at day 21, which was 1581.76 μm. At day 21, the cell-laden scaffold group had the shortest wound length, measuring 1504.15 μm. These results indicated that the cell-laden scaffold can accelerate wound closure and accelerate the repair of full-thickness skin defects.

During the remodeling phase of wound healing, the deposition and distribution of collagen serve as critical indicators of the efficiency of wound healing [52]. But the excessive production and deposition of collagen can increase the scar volume, leading to the formation of scar tissue [53]. As shown in Fig. 7b, MT staining demonstrated that the hydrogel and cell-laden scaffold groups had more extensive collagen deposition than the control group at days 7 and 14. However, at day 21, a larger area of collagen deposition was found in the wound site of the control group, indicating a higher rate of scar formation. In contrast, wounds treated with the cell-laden scaffold group exhibited neatly aligned and loose collagen fibers, which is more similar to natural skin. Through quantitative analysis, it was found that the group treated with the cell-laden scaffold demonstrated the lowest collagen fraction at 21 days (Fig. 7e). These results suggested that this scaffold contributes to normalize skin regeneration and avoids scarring.

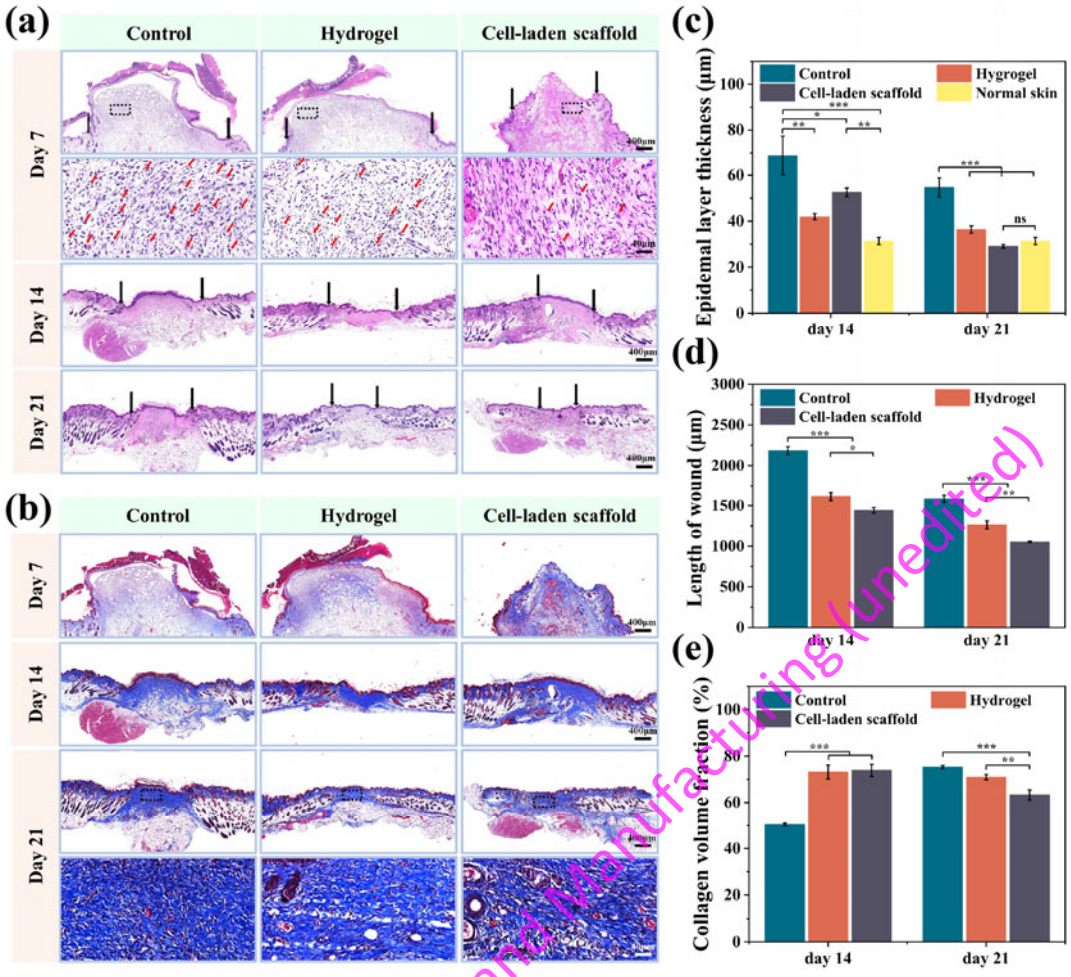

Fig. 7 Analysis of wound healing through H&E staining and Masson staining. **(a)** Evaluation of wound site through H&E staining at 7, 14, and 21 days, with black arrows indicating wound gaps; **(b)** Evaluation of wound site through MT staining at 7, 14, and 21 days, Scale bars: 400 μm for low magnification and 40 μm for high magnification; **(c)** Epidermal thickness at the wound site at 14 and 21 days, compared to normal skin; **(d)** Wound length at 14 and 21 days, measured based on H&E staining results; **(e)** Collagen volume fraction at 14 and 21 days after treatment, determined through analysis of MT staining, where light blue represents collagen deposition. For statistical significance: ns $\geqslant$ 0.5, *p < 0.05, **p < 0.01 and ***p < 0.001.

CK14 serves as a key marker of the stratified epithelium in healthy skin. It is mainly expressed in basal layer epithelial cells and gradually decreases in expression as cells undergo differentiation and migrate away from the basal layer. On the other hand, CK10 is a late-stage marker of epidermal differentiation, commonly observed in the upper layers of the epidermis [54]. Immunohistochemical staining was utilized to examine the expression levels of both CK14 and CK10 proteins, allowing for the

assessment of the degree of epidermal differentiation present at the site of injury. As shown in Fig. 8a and b, both the cell-laden scaffold and hydrogel groups exhibited widespread distribution of CK14 and CK10 positive cells throughout the entire upper cortex after 14 days of treatment, in contrast to the negativity observed in the control group. At 21 days, CK14 expression was found to be robustly expressed in all test groups, while CK10-positive cells were predominantly concentrated in the upper basal layer of the cell-laden scaffold and hydrogel groups, with only weak and sporadic expression was observed in the control group. The observed differential expression indicates a synergistic effect of the combination of COS and GelMA in promoting fibroblast/keratinocyte proliferation and migration, thereby further supporting rapid wound healing and re-epithelialization.

When the skin is damaged, many cellular activities are regulated by cytokines, primarily regulating the metabolism and proliferation of cells surrounding the wound [55]. Tumor necrosis factor-α (TNF-α) is a typical pro-inflammatory factor and one of the markers of inflammation [56]. The immunohistochemical staining results of TNF-α (Fig. 8c) demonstrated that both the hydrogel group and cell-laden scaffold group displayed reduced levels of TNF-α expression compared to the control group at 14-day and 21-day time points. Moreover, the cell-laden scaffold group exhibited the lowest level of expression among the three groups. This outcome can be attributed to the anti-inflammatory properties conferred by the addition of COS to the hydrogel. Moreover, Blood vessel formation is essential for wound repair as it aids in the formation of granulation tissue and provides nutrients and oxygen required for the healing process [57]. The degree of blood vessel formation at the site of injury was evaluated via immunohistochemical staining of CD31 and α-smooth muscle actin (α-SMA) (Fig. 8d, e). After a period of 21 days, the results demonstrated that the hydrogel group and cell-laden scaffold group exhibited notably elevated levels of CD31 and α-SMA positive cells compared to the control group. Notably, the cell-laden scaffold group demonstrated the most pronounced effect among the experimental groups indicated the pro-angiogenesis of the cell-laden scaffold for accelerating wound healing. This may be attributable to the ability of GelMA to provide a supportive microenvironment for

blood vessel formation [58]. Furthermore, COS plays a significant role in inducing repair-promoting macrophages to produce VEGF, which lead to the formation of new blood vessels [30].

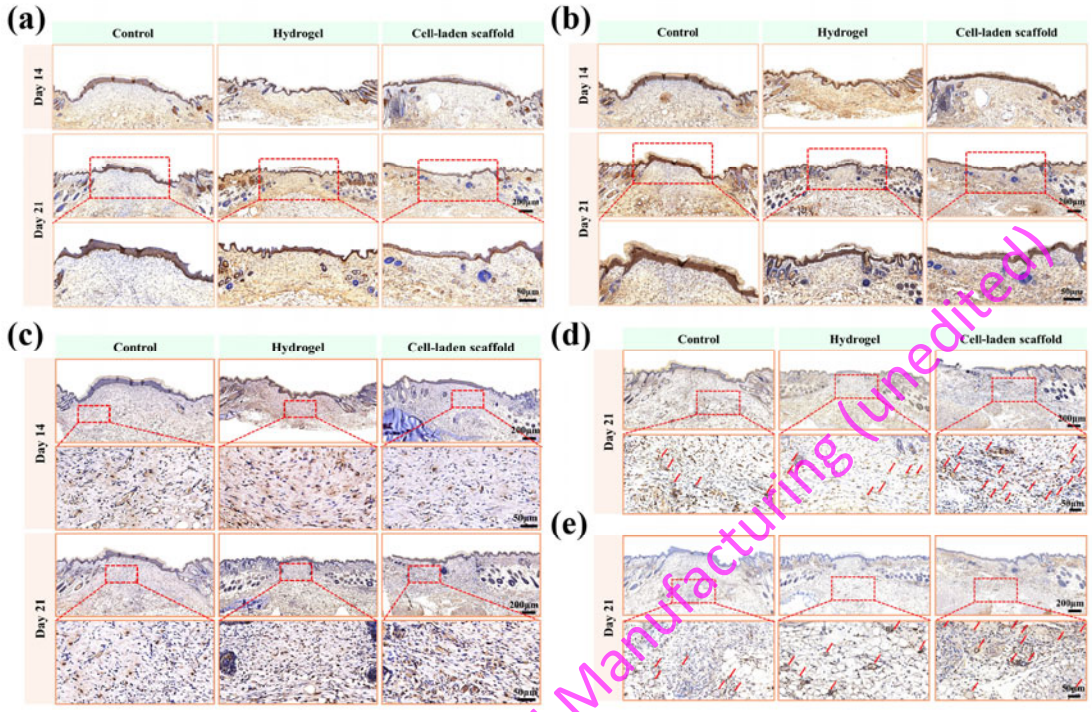

Fig. 8 Immunohistochemical staining of the wound site. **(a)** Staining of CK10 at 14 and 21 days; **(b)** Staining of CK14 at 14 and 21 days; **(c)** Staining of TNF-α at 14 and 21 days; **(d)** Staining of CD31 at 21 days, with red arrows indicating vascular networks with endothelial cells; **(e)** Staining of α-SMA at 21 days, with red arrows representing vascular networks with smooth muscle cells. Scale bars: 200 μm for low magnification and 50 μm for high magnification.

4. Conclusion

This study developed a GelMA/COS composite bioink and rapidly constructed a cell-laden dermal scaffold using DLP printing technology. The GelMA/COS bioink exhibited excellent swelling, degradation performance, mechanical properties and cell compatibility. Furthermore, the bioink demonstrated notable antibacterial activity against both E. coli and S. aureus. The cell-laden dermal scaffold possessed shape stability as well as long-term cellular viability. In vivo experiments further demonstrated that the cell-laden scaffold can accelerate wound closure rate, reduce inflammatory response, enhance angiogenesis, and improve wound healing quality. To

summarize, this dermal scaffold is easy to manufacture and effectively promotes skin tissue regeneration, showing potential for clinical applications. Nonetheless, given the substantial differences in wound healing processes between humans and mice, further exploration of its applicability and regenerative effects in large wounds necessitates the use of a porcine model.

Author Contributions

Lu Han: Conceptualization, Investigation, Methodology, Writing original draft, Validation, Data curation. Zixian Liu: Writing-review & editing. Meng Li: Validation, Writing-review & editing. Zhizhong Shen: Validation, Investigation. Shengbo Sang: Conceptualization, Writing-review & editing, Supervision, Funding acquisition. Jianming Wang: Methodology, Validation, Writing review & Editing.

Declaration of Competing Interest

The authors declare that they have no known competing financial interests or personal relationships that could have appeared to influence the work reported in this paper.

Acknowledgements

This work was supported by the National Natural Science Foundation of China (No. 51975400, No. 62031022), Shanxi Provincial Key Medical Scientific Research Project (2020XM06), Shanxi Provincial Basic Research Project (No. 202103021221006, No. 20210302123040, No. 202103021223069), Scientific and Technological Innovation Programs of Higher Education Institutions in Shanxi (No. 2021L044), Shanxi-Zheda Institute of Advanced Materials and Chemical Engineering (2022SX-TD026).

References

[1] T.T. Nyame, H.A. Chiang, T. Leavitt, M. Ozambela, D.P. Orgill, Tissue-Engineered Skin Substitutes, Plastic and Reconstructive Surgery 136(6) (2015) 1379-1388. http://dx.doi.org/10.1097/prs.0000000000001748

[2] L. Wei, J. Tan, L. Li, H. Wang, S. Liu, J. Chen, Y. Weng, T. Liu, Chitosan/Alginate Hydrogel Dressing Loaded FGF/VE-Cadherin to Accelerate Full-Thickness Skin Regeneration and More Normal Skin Repairs, Int J Mol Sci 23(3) (2022). http://dx.doi.org/10.3390/ijms23031249

[3] S.O. Blacklow, J. Li, B.R. Freedman, M. Zeidi, C. Chen, D.J. Mooney, Bioinspired mechanically active adhesive dressings to accelerate wound closure, Science Advances 5(7) (2019). http://dx.doi.org/10.1126/sciadv.aaw3963

[4] H. Wang, D. Sun, W. Lin, C. Fang, K. Cheng, Z. Pan, D. Wang, Z. Song, X. Long, One-step fabrication of cell sheet-laden hydrogel for accelerated wound healing, Bioactive Materials 28 (2023) 420-431. http://dx.doi.org/10.1016/j.bioactmat.2023.06.005

[5] D.M. Supp, S.T. Boyce, Engineered skin substitutes: practices and potentials, Clinics in Dermatology 23(4) (2005) 403-412. http://dx.doi.org/10.1016/j.clindermatol.2004.07.023

[6] S.R. Gomes, G. Rodrigues, G.G. Martins, M.A. Roberto, M. Mafra, C.M.R. Henriques, J.C. Silva, In vitro and in vivo evaluation of electrospun nanofibers of PCL, chitosan and gelatin: A comparative study, Materials Science and Engineering: C 46 (2015) 348-358. http://dx.doi.org/10.1016/j.msec.2014.10.051

[7] T.M. Quynh, H. Mitomo, N. Nagasawa, Y. Wada, F. Yoshii, M. Tamada, Properties of crosslinked polylactides (PLLA & PDLA) by radiation and its biodegradability, European Polymer Journal 43(5) (2007) 1779-1785. http://dx.doi.org/10.1016/j.eurpolymj.2007.03.007

[8] Z. Zhang, C. Huang, S. Guan, L. Wang, H. Yin, J. Yin, J. Liu, J. Wu, Hybrid gelatin-ascorbyl phosphate scaffolds accelerate diabetic wound healing via ROS scavenging, angiogenesis and collagen remodeling, Biomaterials Advances 158 (2024). http://dx.doi.org/10.1016/j.bioadv.2024.213779

[9] P. Xin, S. Han, J. Huang, C. Zhou, J. Zhang, X. You, J. Wu, Natural okra-based hydrogel for chronic diabetic wound healing, Chinese Chemical Letters 34(8) (2023). http://dx.doi.org/10.1016/j.cclet.2022.108125

[10] H. Zhong, J. Huang, M. Luo, Y. Fang, X. Zeng, J. Wu, J. Du, Near-field electrospun PCL fibers/GelMA hydrogel composite dressing with controlled deferoxamine-release ability and retiform surface for diabetic wound healing, Nano Research 16(1) (2022) 599-612. http://dx.doi.org/10.1007/s12274-022-4813-5

[11] X. Wang, Z. Liu, Q. Duan, B. Zhang, Y. Cao, Z. Shen, M. Li, Y. Xi, J. Wang, S. Sang, 3D bioprinting of in vitro porous hepatoma models: establishment, evaluation, and anticancer drug testing, Bio-Design and Manufacturing 7(2) (2023) 137-152. http://dx.doi.org/10.1007/s42242-023-00263-1

[12] Y. Guo, J. Huang, Y. Fang, H. Huang, J. Wu, 1D, 2D, and 3D scaffolds promoting angiogenesis for enhanced wound healing, Chemical Engineering Journal 437 (2022). http://dx.doi.org/10.1016/j.cej.2022.134690

[13] M. Askari, M. Afzali Naniz, M. Kouhi, A. Saberi, A. Zolfagharian, M. Bodaghi, Recent progress in extrusion 3D bioprinting of hydrogel biomaterials for tissue regeneration: a comprehensive review with focus on advanced fabrication techniques, Biomaterials Science 9(3) (2021) 535-573. http://dx.doi.org/10.1039/d0bm00973c

[14] L. Li, C. Lu, L. Wang, M. Chen, J. White, X. Hao, K.M. McLean, H. Chen, T.C. Hughes, Gelatin-Based Photocurable Hydrogels for Corneal Wound Repair, ACS Applied Materials & Interfaces 10(16) (2018) 13283-13292. http://dx.doi.org/10.1021/acsami.7b17054

[15] R.E. Saunders, B. Derby, Inkjet printing biomaterials for tissue engineering: bioprinting, International Materials Reviews 59(8) (2014) 430-448. http://dx.doi.org/10.1179/1743280414y.0000000040

[16] H. Hong, Y.B. Seo, D.Y. Kim, J.S. Lee, Y.J. Lee, H. Lee, O. Ajiteru, M.T. Sultan, O.J. Lee, S.H. Kim, C.H. Park, Digital light processing 3D printed silk fibroin hydrogel for cartilage tissue engineering, Biomaterials 232 (2020). http://dx.doi.org/10.1016/j.biomaterials.2019.119679

[17] S.H. Kim, Y.K. Yeon, J.M. Lee, J.R. Chao, Y.J. Lee, Y.B. Seo, M.T. Sultan, O.J. Lee, J.S. Lee, S.-i. Yoon, I.-

S. Hong, G. Khang, S.J. Lee, J.J. Yoo, C.H. Park, Precisely printable and biocompatible silk fibroin bioink for digital light processing 3D printing, Nature Communications 9(1) (2018). http://dx.doi.org/10.1038/s41467-018-03759-y

[18] W. Zhu, X. Qu, J. Zhu, X. Ma, S. Patel, J. Liu, P. Wang, C.S.E. Lai, M. Gou, Y. Xu, K. Zhang, S. Chen, Direct 3D bioprinting of prevascularized tissue constructs with complex microarchitecture, Biomaterials 124 (2017) 106-115. http://dx.doi.org/10.1016/j.biomaterials.2017.01.042

[19] Y. Shen, H. Tang, X. Huang, R. Hang, X. Zhang, Y. Wang, X. Yao, DLP printing photocurable chitosan to build bio-constructs for tissue engineering, Carbohydrate Polymers 235 (2020). http://dx.doi.org/10.1016/j.carbpol.2020.115970

[20] L.-H. Han, S. Suri, C.E. Schmidt, S. Chen, Fabrication of three-dimensional scaffolds for heterogeneous tissue engineering, Biomedical Microdevices 12(4) (2010) 721-725. http://dx.doi.org/10.1007/s10544-010-9425-2

[21] A.C. Daly, S.E. Critchley, E.M. Rencsok, D.J. Kelly, A comparison of different bioinks for 3D bioprinting of fibrocartilage and hyaline cartilage, Biofabrication 8(4) (2016). http://dx.doi.org/10.1088/1758-5090/8/4/045002

[22] M.Y. Shie, J.J. Lee, C.C. Ho, S.Y. Yen, H.Y. Ng, Y.W. Chen, Effects of Gelatin Methacrylate Bio-ink Concentration on Mechano-Physical Properties and Human Dermal Fibroblast Behavior, Polymers (Basel) 12(9) (2020). http://dx.doi.org/10.3390/polym12091930

[23] R.I. RI, R. do Amaral, R.L. Reis, A.P. Marques, C.M. Murphy, F.J. O'Brien, 3D-Printed Gelatin Methacrylate Scaffolds with Controlled Architecture and Stiffness Modulate the Fibroblast Phenotype towards Dermal Regeneration, Polymers (Basel) 13(15) (2021). http://dx.doi.org/10.3390/polym13152510

[24] V.K. Mourya, N.N. Inamdar, Y.M. Choudhari, Chitooligosaccharides: Synthesis, characterization and applications, Polymer Science Series A 53(7) (2011) 583-612. http://dx.doi.org/10.1134/s0965545x11070066

[25] T.-S. Vo, C.-S. Kong, S.-K. Kim, Inhibitory effects of chitooligosaccharides on degranulation and cytokine generation in rat basophilic leukemia RBL-2H3 cells, Carbohydrate Polymers 84(1) (2011) 649-655. http://dx.doi.org/10.1016/j.carbpol.2010.12.046

[26] N. Tabassum, S. Ahmed, M.A. Ali, Chitooligosaccharides and their structural-functional effect on hydrogels: A review, Carbohydr Polym 261 (2021) 117882. http://dx.doi.org/10.1016/j.carbpol.2021.117882

[27] S. Sang, R. Cheng, Y. Cao, Y. Yan, Z. Shen, Y. Zhao, Y. Han, Biocompatible chitosan/polyethylene glycol/multi-walled carbon nanotube composite scaffolds for neural tissue engineering, Journal of Zhejiang University-SCIENCE B 23(1) (2022) 58-73. http://dx.doi.org/10.1631/jzus.B2100155

[28] G.-W. Oh, S.-C. Kim, T.-H. Kim, W.-K. Jung, Characterization of an oxidized alginate-gelatin hydrogel incorporating a COS-salicylic acid conjugate for wound healing, Carbohydrate Polymers 252 (2021). http://dx.doi.org/10.1016/j.carbpol.2020.117145

[29] H.-H. Park, S.-C. Ko, G.-W. Oh, Y.-M. Jang, Y.-M. Kim, W.S. Park, I.-W. Choi, W.-K. Jung, Characterization and biological activity of PVA hydrogel containing chitooligosaccharides conjugated with gallic acid, Carbohydrate Polymers 198 (2018) 197-205. http://dx.doi.org/10.1016/j.carbpol.2018.06.070

[30] H. Jafari, K.V. Bernaerts, G. Dodi, A. Shavandi, Chitooligosaccharides for wound healing biomaterials engineering, Mater Sci Eng C Mater Biol Appl 117 (2020) 111266. http://dx.doi.org/10.1016/j.msec.2020.111266

[31] P. Chandika, S.C. Ko, G.W. Oh, S.Y. Heo, V.T. Nguyen, Y.J. Jeon, B. Lee, C.H. Jang, G. Kim, W.S. Park, W.

Chang, I.W. Choi, W.K. Jung, Fish collagen/alginate/chitooligosaccharides integrated scaffold for skin tissue regeneration application, Int J Biol Macromol 81 (2015) 504-13. http://dx.doi.org/10.1016/j.ijbiomac.2015.08.038

[32] Z. Yang, Y. Xi, J. Bai, Z. Jiang, S. Wang, H. Zhang, W. Dai, C. Chen, Z. Gou, G. Yang, C. Gao, Covalent grafting of hyperbranched poly-L-lysine on Ti-based implants achieves dual functions of antibacteria and promoted osteointegration in vivo, Biomaterials 269 (2021) 120534. http://dx.doi.org/10.1016/j.biomaterials.2020.120534

[33] F. Liaqat, R. Eltem, Chitooligosaccharides and their biological activities: A comprehensive review, Carbohydrate Polymers 184 (2018) 243-259. http://dx.doi.org/10.1016/j.carbpol.2017.12.067

[34] C. Kilic Bektas, V. Hasirci, Cell Loaded GelMA:HEMA IPN hydrogels for corneal stroma engineering, J Mater Sci Mater Med 31(1) (2019) 2. http://dx.doi.org/10.1007/s10856-019-6345-4

[35] J.Y. Lai, Y.T. Li, T.P. Wang, In vitro response of retinal pigment epithelial cells exposed to chitosan materials prepared with different cross-linkers, Int J Mol Sci 11(12) (2010) 5256-72. http://dx.doi.org/10.3390/ijms11125256

[36] P. Chandika, G.W. Oh, S.Y. Heo, S.C. Kim, T.H. Kim, M.S. Kim, W.K. Jung, Electrospun porous bilayer nano-fibrous fish collagen/PCL bio-composite scaffolds with covalently cross-linked chitooligosaccharides for full-thickness wound-healing applications, Mater Sci Eng C Mater Biol Appl 121 (2021) 111871. http://dx.doi.org/10.1016/j.msec.2021.111871

[37] D. Dehghan Baniani, R. Bagheri, A. Solouk, Preparation and characterization of a composite biomaterial including starch micro/nano particles loaded chitosan gel, Carbohydrate Polymers 174 (2017) 633-645. http://dx.doi.org/10.1016/j.carbpol.2017.06.095

[38] H. Liu, J. Mao, K. Yao, G. Yang, L. Cui, Y. Cao, A study on a chitosan-gelatin-hyaluronic acid scaffold as artificial skin in vitro and its tissue engineering applications, J Biomater Sci Polym Ed 15(1) (2004) 25-40. http://dx.doi.org/10.1163/156856204322752219

[39] J. Ratanavaraporn, S. Damrongsakkul, S. Kanokpanont, M. Yamamoto, Y. Tabata, Osteogenic Differentiation of Bone-Marrow-Derived Stem Cells Cultured with Mixed Gelatin and Chitooligosaccharide Scaffolds, Journal of Biomaterials Science, Polymer Edition 22(8) (2012) 1083-1098. http://dx.doi.org/10.1163/092050610x499050

[40] F. Nazir, I. Ashraf, M. Iqbal, T. Ahmad, S. Anjum, 6-deoxy-aminocellulose derivatives embedded soft gelatin methacryloyl (GelMA) hydrogels for improved wound healing applications: In vitro and in vivo studies, Int J Biol Macromol 185 (2021) 419-433. http://dx.doi.org/10.1016/j.ijbiomac.2021.06.112

[41] M. Sobota, S. Jurczyk, M. Kwiecien, A. Smola-Dmochowska, M. Musiol, M. Domanski, H. Janeczek, M. Kawalec, P. Kurcok, Crystallinity as a tunable switch of poly(L-lactide) shape memory effects, J Mech Behav Biomed Mater 66 (2017) 144-151. http://dx.doi.org/10.1016/j.jmbbm.2016.11.009

[42] H. Goodarzi, K. Jadidi, S. Pourmotabed, E. Sharifi, H. Aghamollaei, Preparation and in vitro characterization of cross-linked collagen-gelatin hydrogel using EDC/NHS for corneal tissue engineering applications, Int J Biol Macromol 126 (2019) 620-632. http://dx.doi.org/10.1016/j.ijbiomac.2018.12.125

[43] D. Puppi, F. Chiellini, A.M. Piras, E. Chiellini, Polymeric materials for bone and cartilage repair, Progress in Polymer Science 35(4) (2010) 403-440. http://dx.doi.org/10.1016/j.progpolymsci.2010.01.006

[44] J. He, Y. Liang, M. Shi, B. Guo, Anti-oxidant electroactive and antibacterial nanofibrous wound dressings based on poly(ε-caprolactone)/quaternized chitosan-graft-polyaniline for full-thickness skin wound healing, Chemical Engineering Journal 385 (2020). http://dx.doi.org/10.1016/j.cej.2019.123464

[45] Y. Yuan, W. Tan, J. Zhang, Q. Li, Z. Guo, Water-soluble amino functionalized chitosan: Preparation, characterization, antioxidant and antibacterial activities, International Journal of Biological Macromolecules 217 (2022) 969-978. http://dx.doi.org/10.1016/j.ijbiomac.2022.07.187
[46] J.C. Fernandes, F.K. Tavaria, S.C. Fonseca, Ó.S. Ramos, M.E. Pintado, F.X. Malcata, In vitro screening for anti-microbial activity of chitosans and chitooligosaccharides, aiming at potential uses in functional textiles, Journal of Microbiology and Biotechnology 20(2) (2010) 311-318. http://dx.doi.org/10.4014/jmb.0904.04038
[47] J. Zhou, J.-Y. Shen, L.-E. Tao, H. Chen, The Inhibition of Adipose-Derived Stem Cells on the Invasion of Keloid Fibroblasts, International Journal of Medical Sciences 19(12) (2022) 1796-1805. http://dx.doi.org/10.7150/ijms.68646
[48] F. Zahir-Jouzdani, M. Mahbod, M. Soleimani, F. Vakhshiteh, E. Arefian, S. Shahosseini, R. Dinarvand, F. Atyabi, Chitosan and thiolated chitosan: Novel therapeutic approach for preventing corneal haze after chemical injuries, Carbohydrate Polymers 179 (2018) 42-49. http://dx.doi.org/10.1016/j.carbpol.2017.09.062
[49] F. Zhou, Y. Hong, R. Liang, X. Zhang, Y. Liao, D. Jiang, J. Zhang, Z. Sheng, C. Xie, Z. Peng, X. Zhuang, V. Bunpetch, Y. Zou, W. Huang, Q. Zhang, E.V. Alakpa, S. Zhang, H. Ouyang, Rapid printing of bio-inspired 3D tissue constructs for skin regeneration, Biomaterials 258 (2020) 120287. http://dx.doi.org/10.1016/j.biomaterials.2020.120287
[50] L. Deng, H. Lu, C. Tu, T. Zhou, W. Cao, C. Gao, A tough synthetic hydrogel with excellent post-loading of drugs for promoting the healing of infected wounds in vivo, Biomater Adv 134 (2022) 112577. http://dx.doi.org/10.1016/j.msec.2021.112577
[51] Z. Wu, Y. Hong, Combination of the Silver–Ethylene Interaction and 3D Printing To Develop Antibacterial Superporous Hydrogels for Wound Management, ACS Applied Materials & Interfaces 11(37) (2019) 33734-33747. http://dx.doi.org/10.1021/acsami.9b14090
[52] J. Wu, Z. Xiao, A. Chen, H. He, C. He, X. Shuai, X. Li, S. Chen, Y. Zhang, B. Ren, J. Zheng, J. Xiao, Sulfated zwitterionic poly(sulfobetaine methacrylate) hydrogels promote complete skin regeneration Acta Biomater 71 (2018) 293-305. http://dx.doi.org/10.1016/j.actbio.2018.02.034
[53] B. Yuan, Z. Upton, D. Leavesley, C. Fan, X.Q. Wang, Vascular and Collagen Target: A Rational Approach to Hypertrophic Scar Management, Adv Wound Care (New Rochelle) 12(1) (2023) 38-55. http://dx.doi.org/10.1089/wound.2020.1348
[54] L.W. Jiang, H. Chen, H. Lu, Using human epithelial amnion cells in human de-epidermized dermis for skin regeneration, J Dermatol Sci 81(1) (2016) 26-34. http://dx.doi.org/10.1016/j.jdermsci.2015.10.018
[55] T. Kondo, Y. Ishida, Molecular pathology of wound healing, Forensic Science International 203(1-3) (2010) 93-98. http://dx.doi.org/10.1016/j.forsciint.2010.07.004
[56] Y. Yang, Y. Liang, J. Chen, X. Duan, B. Guo, Mussel-inspired adhesive antioxidant antibacterial hemostatic composite hydrogel wound dressing via photo-polymerization for infected skin wound healing, Bioactive Materials 8 (2022) 341-354. http://dx.doi.org/10.1016/j.bioactmat.2021.06.014
[57] J. Li, Y.P. Zhang, R.S. Kirsner, Angiogenesis in wound repair: angiogenic growth factors and the extracellular matrix, Microsc Res Tech 60(1) (2003) 107-14. http://dx.doi.org/10.1002/jemt.10249
[58] Y.C. Chen, R.Z. Lin, H. Qi, Y. Yang, H. Bae, J.M. Melero-Martin, A. Khademhosseini, Functional Human Vascular Network Generated in Photocrosslinkable Gelatin Methacrylate Hydrogels, Adv Funct Mater 22(10) (2012) 2027-2039. http://dx.doi.org/10.1002/adfm.201101662